

Bright and Polarized Fiber In-Line Single-Photon Source Based on Plasmon-Enhanced Emission into Nanofiber Guided Modes

K. Muhammed Shafi^{1,2,3}, Ramachandrarao Yalla⁴, and Kali P. Nayak^{1,5,*}


¹Center for Photonic Innovations and Institute for Laser Science, University of Electro-Communications, Tokyo 182-8585, Japan

²Deltafiber.jp Ltd., Yaehara, Tomi-shi, Nagano 389-0406, Japan

³Department of Instrumentation and Applied Physics, Indian Institute of Science, Bengaluru 560012, India

⁴School of Physics, University of Hyderabad, Hyderabad, Telangana 500046, India

⁵Department of Engineering Science, University of Electro-Communications, Tokyo 182-8585, Japan

 (Received 25 June 2022; revised 10 October 2022; accepted 24 January 2023; published 2 March 2023)

We demonstrate a bright and polarized fiber in-line single-photon source based on plasmon-enhanced emission of colloidal single quantum dots into an optical nanofiber. We show that emission properties of single quantum dots can be strongly enhanced in the presence of single gold nanorods leading to a bright and strongly polarized single-photon emission. The single photons are efficiently coupled to guided modes of the nanofiber and eventually to a single-mode optical fiber. The brightness (fiber-coupled photon count rate) of the single-photon source is estimated to be 12.2 ± 0.6 MHz, with high single-photon purity [$g^2(0) = 0.20 \pm 0.04$] and degree of polarization as high as 94–97%. The polarized and fiber-coupled single photons can be implemented for potential applications in quantum photonics.

DOI: [10.1103/PhysRevApplied.19.034008](https://doi.org/10.1103/PhysRevApplied.19.034008)

I. INTRODUCTION

The development of efficient single-photon sources (SPSs) is central to the realization of quantum networks and quantum information science [1–4]. A straightforward approach to generate single photons is to collect the emission from a single quantum emitter [5,6]. However, there are two key challenges in this approach. One is the emission properties of the quantum emitter and the other is efficient collection of emitted single photons in a single spatial mode preferably into a single-mode optical fiber (SMF).

The requirements as a quantum emitter for an efficient SPS is that it must be bright, producing a high photon count rate and with a high degree of polarization (DOP). High photon count rate is essential to match the requirements for high data rates. High DOP is also crucial as many protocols require information to be encoded as polarization qubits [7,8]. In this context, solid-state quantum emitters like quantum dots (QDs) or atomlike defects in crystalline hosts [5,6,8,9] are one of the promising choices for practical SPS, based on the emission properties brighter than neutral atoms or ions and easier techniques to isolate single emitters. However, the presence of the complex mesoscopic solid-state host induces various challenges, e.g.,

inhomogeneous spectral broadening, emission intermittency and reduced DOP, etc. In the last decade, there have been significant efforts and developments to overcome such issues [5,6,10–12].

On the other hand, efficient collection of emitted single photons is an inevitable requirement for high data rates and deterministic communication protocols. In this direction, nanophotonic waveguides and resonators have shown promising advances taking advantage of the strong transverse confinement of photonic modes beyond free-space optics [5,6,13–16]. In particular, metal nanostructures have shown state-of-the-art field confinement leading to strong Purcell enhancement and polarized single-photon emission due to their localized surface plasmon resonance (LSPR) [17–22]. However, the propagation losses in metal waveguides are detrimental. On the other hand, dielectric waveguides have limited field confinement but excellent propagation properties for long-distance communication.

Various methods for collecting single photons from the quantum emitter into the nanophotonic platforms have been successfully demonstrated. However, coupling single photons from nanophotonic platforms to a SMF with high brightness remains challenging [13,14]. Daveau *et al.* and Lee *et al.* demonstrated a fiber-coupled single-photon source-based quantum dot in a photonic waveguide with a brightness of 8.24 and 1.1 MHz, respectively. In another implementation for spectrally narrow single photons based

*kalipnayak@uec.ac.jp

on diamond waveguides, the reported brightness is 0.038 MHz [15].

In this context, tapered optical fiber with subwavelength diameter waist, optical nanofiber (ONF) [23], provides a unique fiber in-line platform for collecting single-emitter fluorescence [24]. The distinct point of the technique is that the guided mode of the ONF can have strong transverse confinement and adiabatically evolve to the SMF mode with near-unity efficiency [25–27]. This provides an automatic and alignment-free fiber-coupled platform for a SPS and easy integration into fiber networks. In the last decade, there has been significant development to interface the ONF platform with various single quantum emitters, which includes laser-cooled atoms [28–31], color centers in nanodiamond [32,33], QDs [34–36], two-dimensional (2D) materials [37], and molecules [38]. Recently, we have reported a fiber in-line SPS based on a hybrid system of colloidal single QDs deposited on an ONF and cooled down to cryogenic temperature (3.7 K). However, the maximum photon count rate and the decay time were limited to 1.6 ± 0.2 MHz and 10.0 ± 0.5 ns, along with limited DOP [39].

Here, we demonstrate a hybrid quantum system by combining a single QD and a single gold nanorod (GNR) coupled to an ONF. We show that emission properties of single QDs can be strongly enhanced in the presence of GNR leading to a bright and strongly polarized single-photon emission. The single photons are efficiently coupled to guided modes of the ONF and eventually to a SMF. The brightness (fiber-coupled photon count rate) of the SPS is estimated to be 12.2 ± 0.6 MHz, with high single-photon purity ($g^2(0) = 0.20 \pm 0.04$) and DOP as high as 94–97%.

II. NUMERICAL SIMULATIONS

A schematic diagram of the hybrid quantum system is shown in Fig. 1(a). The hybrid quantum system is formed by combining a single QD and GNR with an ONF. Using the finite-difference time-domain (FDTD) method, we simulate the field profile, Purcell enhancement factor (PF), emission enhancement factor into guided modes (EF), and DOP of the emitted photons into ONF guided modes by placing a single dipole source (DS) close to the surface of the GNR. The ONF is a silica cylinder of 320 nm in diameter, and the GNR is a gold rod with hemispherical end caps, with a length of 75 nm and a diameter of 30 nm. The GNR is placed on the ONF with its axis parallel to the ONF axis, and the DS is placed 5 nm away from surface of the GNR to mimic the experimental conditions (considering the size of a thick-shell QD). The DS wavelength is chosen from 550 to 750 nm. The PF is determined by Γ/Γ_0 , where Γ (Γ_0) is the total decay rate in the presence (absence) of GNR and ONF. The EF is determined by I^c/I^{un} , where I^c and I^{un} are the intensities of the emitted light coupled to the ONF in the presence and absence of the GNR, respectively.

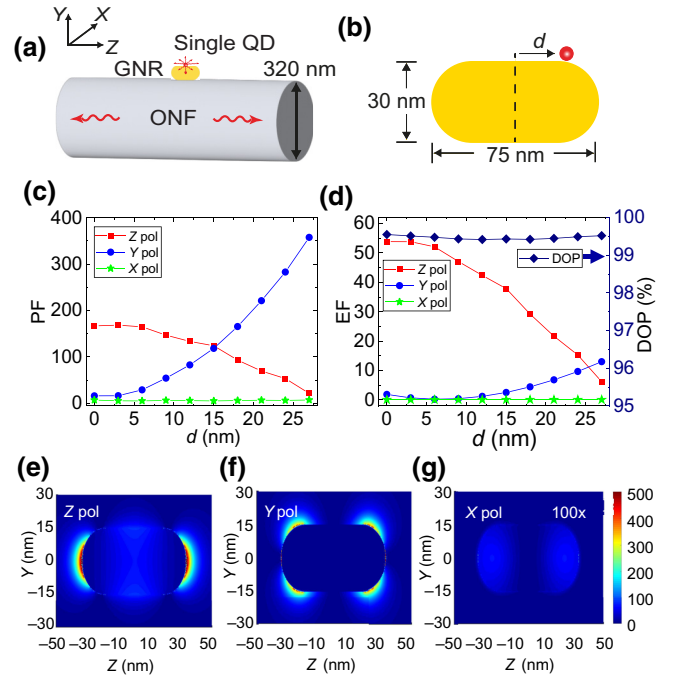


FIG. 1. Numerical simulations of the system. (a) Schematic illustration of the hybrid system based on single CdSe/ZnS QD coupled to a single GNR on ONF. (b) Schematic of the emitter position (d) along the GNR axis. (c) Simulated PF for Z, Y, and X polarization of the emitted photons into ONF. (d) EF and DOP of the emitted photons into ONF guided modes. (e), (f), (g) Simulated scattering-field profiles for Z, Y, and X polarization, respectively.

We perform the simulations for three polarization orientations (X, Y, and Z pol) of the DS. The DOP is determined by $(I_Y^c + I_Z^c - I_X^c)/(I_Y^c + I_Z^c + I_X^c)$, where I_i^c ($i = X, Y, Z$) is the intensity of the emitted light coupled to the ONF in the presence of GNR, for a dipole polarized along the i axis. The DOP is defined based on the polarization distribution of the ONF guided modes [40,41].

The simulations are performed by varying the DS position along the axis (Z axis) of the GNR [as illustrated in Fig. 1(b)]. Figures 1(c) and 1(d) show the PF and EF values for various dipole source positions (d) from the center of the GNR. The red circles, blue squares, and green stars show the values for Z-, Y-, and X-pol dipole orientations, respectively. One can readily see that for Z pol, the PF (EF) is highest at $d = 0$ nm with a value around 169 (53) and decreases as d increases. They reach a minimum at around the edge ($d = 27$ nm). On the other hand, for Y pol the PF (EF) is lowest at the center and increases towards the edge with a maximum value of 359 (13). In contrast, for X pol the PF (EF) are extremely small compared to the Z and Y pol at all positions. The black diamonds in Fig. 1(d) show the DOP at respective positions. The DOP shows an almost flat trend with a value $> 99\%$ at all positions.

In order to understand the field enhancement due to the LSPR, we simulate the scattering-field profile around the GNR. The simulated field profile for Z , Y , and X pol are shown in Figs. 1(e), 1(f) and 1(g), respectively. One can see that for Z pol the field enhancement is maximum at the tips of the GNR as well as at its center ($d = 0$ nm). One can readily see that the field enhancement decreases as d increases. The enhancement at the tips is 4–5 times stronger than the center. On the other hand, for Y pol the field enhancement is strongest at the edges and decreases and reaches minimum towards the center and tips. In contrast, for X pol the field enhancement is extremely weak compared to Z and Y pol. This trend qualitatively explains the simulation results shown in Figs. 1(c) and 1(d).

III. EXPERIMENTAL METHODS

Figure 2(a) shows the schematic diagram of the experiment. The experimental setup is based on a hybrid system of a single QD and a GNR deposited on an ONF. ONFs with optical transmission of $>99\%$ are fabricated using a commercially available machine (Taper Fiber Expert, Deltafiber.jp Ltd., Japan) by adiabatically tapering SMFs (SM 600, Fibercore) using a heat and pull technique. ONFs used for the experiment had a waist diameter of 310 ± 10 nm and a uniform waist length of 2.5 mm. The ONF diameter is chosen to maximize the channeling of the single QD emission into the ONF guided modes [24,35]. The QDs used for the experiment are thick-shell CdSe/ZnS QDs dispersed in toluene colloidal solution [42]. At room temperature, the QDs emit at a wavelength of 640 nm. The GNRs (E12-25-650, Nanopartz) used for the experiment are also dispersed in a toluene colloidal solution. The quoted diameter and length of the GNR are 25 and 71 nm, respectively. The quoted center wavelength of the LSPR of GNRs is 650 nm with a spectral width of around 100 nm FWHM.

The procedure for the sample preparation is as follows. The GNRs and QDs are deposited together on the ONF using a computer-controlled subpicoliter needle-dispenser (SPLD) system [43] installed on an inverted microscope (Nikon, Eclipse Ti-U)). The dispenser consists of a tapered glass tube containing GNR and QD mixed in a toluene colloidal solution and a tungsten needle with a tip diameter of 5 μm . Once the computer-controlled needle tip passes through the glass tube, it carries a small amount of GNR and QD mixed solution at its edge and a tiny amount of this solution is deposited on the ONF surface by bringing the tip into contact with the ONF. A laser is introduced into the ONF to monitor the deposition process. To get a single GNR and single QD on the ONF, we first optimize the concentration of GNR to be 10^{10} rods/ cm^3 and that of QD to be 10^{13} dots/ cm^3 . The success probability of deposition of a single GNR and single QD on the ONF for each trail is about 60 %.

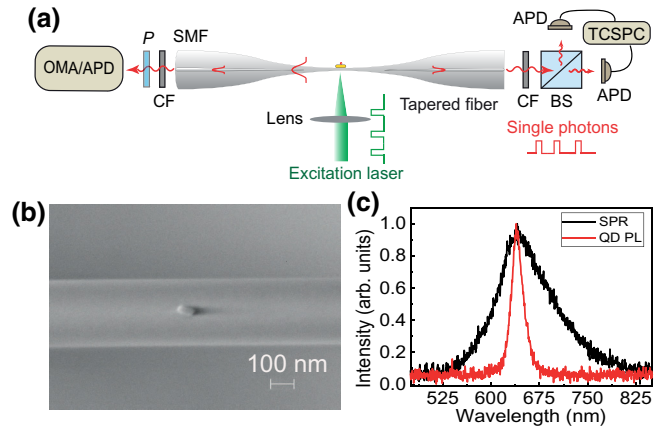


FIG. 2. Experimental setup. (a) Schematic diagram of the hybrid system. A single CdSe/ZnS QD on a single GNR is interfaced with the ONF. The single QD is excited using a cw or a pulsed laser and the emission from the single QD is coupled to the guided mode of the ONF and eventually to a single-mode optical fiber (SMF). The temporal, spectral, and polarization characteristics of the fiber-guided photons are measured at either end of the fiber. The abbreviations denote the following: CF, color glass filter; BS, beam splitter; APD, avalanche photodiode (single-photon counting module); TCSPC, time-correlated single-photon counter; P , polarizer; OMA, optical multichannel spectrum analyzer. (b) A typical SEM image of single GNR and single QD deposited on ONF. (c) The black and red traces show the spectrum of light scattered by GNR revealing the LSPR of GNR and the PL spectrum of single QD, respectively.

Figure 2(a) shows the measurement scheme of the experiment. Note that all experiments are performed at room temperature. The emission characteristics of the both coupled (GNR+QD) and uncoupled (only QD) single QDs are investigated via the guided mode of the ONF and eventually through a SMF. The single QDs are excited using a cw or a pulsed frequency-doubled YAG laser at a wavelength of 532 nm. The pulse width of the pulsed-laser is 20 ps. The excitation laser is linearly polarized with a polarization perpendicular to the ONF axis and laser is focused to a spot size of 1 μm using a microscope objective lens.

The photoluminescence (PL) from the single QDs is measured through the guided mode of the optical fiber on both sides of the ONF. The scattered excitation laser light is filtered using a 560 nm long-pass color glass filter [CF; (O56, HOYA)]. Photons from one side of the fiber are used for spectral measurements using an optical multichannel spectrum analyzer (OMA). The same side is also used for emission polarization measurements. A fiber in-line polarization controller [not shown in Fig. 2(a)] and a linear polarizer (P) is introduced in the path to the avalanche photodiode (APD) for the polarization measurements. The fiber in-line polarization controller is used to compensate for the birefringence induced by the ONF and other fiber loops before the free-space outcoupling. It should be noted

that for the LSPR spectrum measurements, the GNR on the ONF is irradiated with a white-light source and the scattered light is measured through the ONF without CF.

Photons channeled into the other side of the fiber are used to measure the temporal characteristics. A Hanbury Brown-Twiss (HBT) scheme is employed for photon correlation measurements, in which photons emitted from the QD are split using a 50:50 nonpolarizing beam splitter and detected by two fiber-coupled APDs. The arrival times of the photons are recorded using a time-correlated single-photon counter (PicoHarp 300, Pico Quant GmbH) for deriving the photon correlations. PL decay curves are obtained by measuring correlations between excitation sync pulse and arrival times of emitted photons.

IV. RESULTS

Figure 2(b) shows a typical scanning electron microscope (SEM) image of the single GNR and single QD on the ONF. One can clearly see a single GNR on the surface of the ONF aligned almost parallel to the ONF axis. From the different trails, we estimate an average angle of $\pm 20^\circ$ with respect to the ONF axis. From the SEM images, we estimate the size distribution of the GNR to be 71 ± 4 in length and 31 ± 2 nm in diameter. Note that the single QD is less than 10 nm in size and is not visible in the SEM image.

The black trace in Fig. 2(c) shows the spectrum of light scattered by the GNR. One can clearly see a peak around 640 nm revealing the LSPR of the GNR. The FWHM of the LSPR spectrum is around 106 nm. The red trace in Fig. 2(c) shows the PL spectrum of the single QD on the ONF. The center wavelength of the PL spectrum is 640 nm that matches to the LSPR peak and it has a FWHM of 19.6 nm that is well within the LSPR. The measured distribution of central wavelengths of QD and LSPR are 640 ± 3 and 640 ± 5 nm, respectively.

Figure 3 summarizes the temporal characteristics of emission from coupled and uncoupled QDs on an ONF. We measure the photon correlations $g^2(\tau)$ of the PL emission into the ONF to confirm that the emission is from a single QD. The red and black traces in Fig. 3(a) show the normalized photon correlation $g^2(\tau)$ of the PL emission from coupled and uncoupled QDs, respectively, while excited with the 532-nm cw laser at an excitation intensity of 6 W/cm^2 . The solid curves in Fig. 3(a) are the exponential fit for $g^2(\tau)$ [43]. One can clearly see the antibunching behavior for both coupled and uncoupled QDs indicating that the emission is indeed from single QDs. The $g^2(0)$ values for the coupled and uncoupled cases are 0.43 ± 0.03 and 0.07 ± 0.02 , respectively. The rise times of the antibunching signals for the coupled and uncoupled QDs are 2.5 ± 0.2 and 55 ± 2 ns, respectively. This indicates the strong Purcell enhancement for the coupled QD. However,

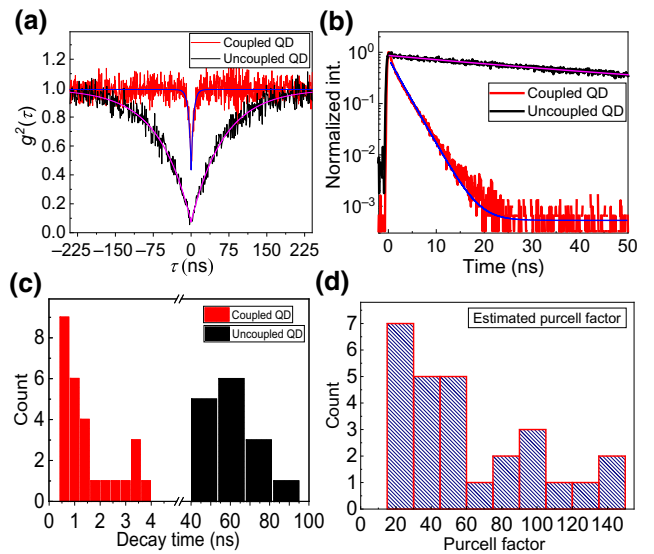


FIG. 3. Temporal characteristics of the PL emission. (a) Normalized photon correlation $g^2(\tau)$ for coupled (red trace) and uncoupled (black trace) single QD, respectively. The solid curves show the exponential fit for the $g^2(\tau)$. (b) PL decay curves for coupled (red trace) and uncoupled (black trace) single QD, respectively. The solid curves show the fits using single exponential functions. (c) Histogram of decay times of coupled (red blocks) and uncoupled (black blocks) single QD, respectively. (d) Histogram of estimated PF for coupled single QDs.

the rise time of the antibunching signal also depends on the intensity of excitation.

To quantify the PF, we measure the PL decay time of the emission. For PL decay measurements, the QDs are excited with a pulsed laser with a repetition rate of 500 kHz and the excitation intensity is 0.2 W/cm^2 . The red and black traces in Fig. 3(b) show the PL decay curves for coupled and uncoupled QDs, respectively. From the single exponential fits to the decay curves, we obtain the decay times (τ_0) of 2.6 ± 0.1 and 61 ± 2 ns for coupled and uncoupled QDs, respectively. The histograms of decay times for coupled and uncoupled QDs for different trials are shown as red and black blocks in Fig. 3(c), respectively. One can clearly see that the decay time for the coupled QDs lies in the range of 0.5 to 4 ns, whereas that for the uncoupled QDs lies in the range of 40 to 90 ns. We estimate an average decay time of uncoupled QDs to be 55 ns with a distribution of ± 10 ns. Using this average value, we estimate the PF for the coupled QDs. The histogram of PF for coupled QDs is plotted in Fig. 3(d). From Fig. 3(d), we infer that the PF lies in the range of 20–140. It should be noted that the distribution of the decay time of uncoupled QDs, induces an error of $\pm 20\%$ in the estimated PF that is much larger than the typical error of $\pm 3\%$ in the measured individual decay times.

Next, we present the polarization properties of the PL emission from coupled and uncoupled QDs on the ONF.

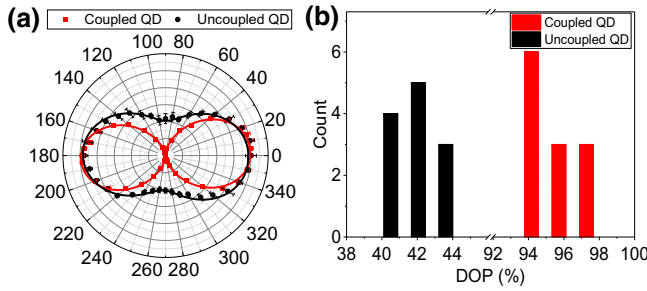


FIG. 4. Emission polarization characteristics of SPS. (a) Emission polarization characteristics of the SPS are indicated in the polar plot, the red data points are for the coupled and black data points are for uncoupled single QD. The solid curves are the cosine-squared fits. (b) Histograms of the degree of polarization (DOP) for coupled (red) and uncoupled (black) single QDs.

The QDs are excited with a polarization perpendicular to the ONF axis and the photon counts through the ONF are measured as a function of the polarizer angle. The red and black data points in Fig. 4(a) show the polar plots for the polarization-resolved normalized photon counts for coupled and uncoupled QDs, respectively. One can clearly see that for the coupled QD, the photon counts are strongly suppressed at an angle of 90° indicating high DOP. The solid curves are the cosine-squared fits. The DOP is estimated from the maximum (N_{\max}) and minimum (N_{\min}) photon counts, as $DOP = (N_{\max} - N_{\min}) / (N_{\max} + N_{\min})$. The red and black blocks in Fig. 4(b) show the histograms of the DOPs for the coupled and uncoupled QDs, respectively. One can see that the DOPs for uncoupled QDs are in the range of 40–44%, whereas the DOPs for the coupled QDs are in the range of 94–97%. This clearly indicates that the DOPs of single QDs can be strongly enhanced due to coupling to localized plasmon field of GNR [22].

Next, we evaluate the system performance as an efficient SPS. The purity of the fiber in-line SPS is estimated by measuring the photon correlations in a pulsed-excitation scheme. The red trace in Fig. 5(a) shows the $g^2(\tau)$ of the coupled single QD measured by exciting the QD using a pulsed laser with 10 MHz repetition rate. The black trace in Fig. 5(a) shows the $g^2(\tau)$ of the uncoupled single QD measured by pulsed excitation at a repetition rate of 2.5 MHz. One can clearly see that for both coupled and uncoupled QDs the central peak at $\tau = 0$, is strongly suppressed indicating high purity single photon characteristics. The single photon purity for the coupled and uncoupled QDs are estimated to be $g^2(0) = 0.20 \pm 0.04$ and 0.07 ± 0.02 , respectively. It should be noted that the reduced decay time for coupled QD enables excitation with a high repetition rate.

The brightness of the SPS is estimated by measuring the intensity dependence of the photon-count rates as shown in Fig. 5(b). The red and black data points in Fig. 5(b) show the photon-count rates for coupled and uncoupled QDs,

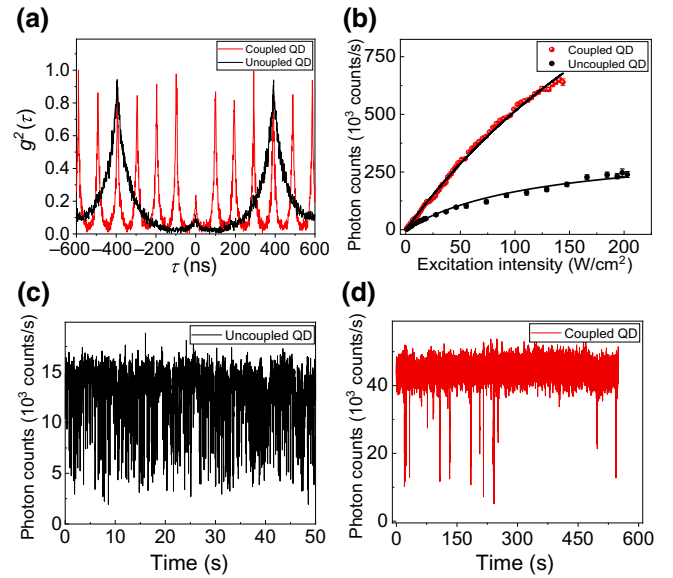


FIG. 5. Single-photon characteristics of SPS. (a) The red trace shows the $g^2(\tau)$ of the coupled single QD measured by exciting the QD using a pulsed laser at 10 MHz. The black trace shows the $g^2(\tau)$ of the uncoupled single QD measured by pulsed excitation at 2.5 MHz (6 W/cm^2). (b) The red and blue data points show the photon-count rate measured through one side of the fiber for coupled and uncoupled single QD, respectively. The solid curves are the fits using the saturation model given in Eq. (1). (c),(d) Photon-count rates for uncoupled and coupled single QDs, respectively. Both are measured with an excitation intensity of 6 W/cm^2 .

respectively. It may be seen that the photon-count rate increases with excitation intensity and shows a saturation behavior for higher excitation intensities. The observations are fitted using a saturation model for the two-level system given as

$$N(F) = N_{\max} \left[\frac{I}{I + I_{\text{sat}}} \right], \quad (1)$$

where N_{\max} is the saturated photon-count rate, I and I_{sat} are the excitation intensity and the saturation intensity, respectively. The solid curves in Fig. 5(b) show the fits. From the fit for the coupled QD (uncoupled QD), we obtain a maximum count rate of single photons at one side of the fiber to be $N_{\max} = 2.50(\pm 0.13) \times 10^6 \text{ counts/s}$ [$0.37(\pm 0.17) \times 10^6 \text{ counts/s}$] and a saturation intensity of $I_{\text{sat}} = 387 \pm 25 \text{ W/cm}^2$ ($122 \pm 9 \text{ W/cm}^2$). Note that the I_{sat} for the coupled QD is higher due to the enhanced decay rate.

The detection efficiency (α) of the optical setup is estimated to be 41%, which includes fiber coupling efficiency from ONF to APD (83%), color glass filter transmission (83%) and detection efficiency of APD at 650 nm (60%). We estimate the brightness (Γ_{SP}) of the SPS (fiber-coupled photon-count rate) as $\Gamma_{\text{SP}} = 2N_{\max}/\alpha$. The factor 2

accounts for the coupling of single photons into both side of the ONF. The Γ_{SP} for the coupled and uncoupled QDs are 12.2 ± 0.6 and 1.8 ± 0.8 MHz, respectively.

We also find that the stability of the photon-count rate is improved for the coupled QDs. Typical photon-count rates for uncoupled and coupled QDs are shown in Figs. 5(c) and 5(d), respectively. The time-axis resolution is 17 ms for both the measurements of 50 s (uncoupled QD) and 600 s (coupled QD). It can be seen that for uncoupled QD well-known strong blinking behavior is observed [22,42], whereas for the coupled QD such blinking behavior is strongly suppressed. This further improves the quality of the SPS.

V. DISCUSSIONS

A key experimental challenge in this work is to interface single GNR-coupled single QDs with ONF. Single QD deposition on ONF is well-established using the SPLD system [35,39,42–44]. However, coupling single QDs to GNR on ONF is challenging. We have tried first depositing single QD and then GNR or vice versa on the ONF. The success probability was very poor and repeated trials led to higher transmission loss of ONF. The procedure presented here works well with a success probability of 60% for depositing a single QD coupled to a single GNR on the ONF. The typical transmission drop of ONF for each deposition is 1.4%.

From the PF estimation in Fig. 3(d), it is inferred that the PF is in the range of 20–140. The upper limit of the estimated PF may be attributed to the timing resolution of 290 ps of the detection system. The observed Purcell enhancement reasonably lies in the range as expected from the numerical simulations shown in Fig. 1(b). The distribution of the PF may correspond to the different polarization orientation and position of the QD on GNR for different trials. One may further use sophisticated nanomanipulation techniques [32,33] for deterministic positioning of single QD and GNR. Note that the observed Purcell enhancement is much higher than that reported for ONF cavities [29,30,44,45]. Moreover, it is broadband enhancement covering the entire PL spectrum, useful for room-temperature-based SPS.

Apart from strong Purcell enhancement, another dramatic effect is the strong enhancement of DOP. As shown in Fig. 4(b), the DOPs can be as high as 94–97%. This also agrees well with the numerical simulations shown in Fig. 1(b). The discrepancies can be attributed to the typical error in the measured photon-count rate and imperfect compensation of birefringence induced by ONF and other fiber loops. The single photons coupled to the fiber-guided modes are strongly polarized along the transverse axis containing the QD and the GNR. Such high DOP is essential for room-temperature-based SPS.

From the Γ_{SP} of the coupled and uncoupled QDs [discussed in Fig. 5(b)], we estimate an EF of 6.8 for the coupled QD. From the PL decay times shown in Fig. 3(b), the PF for the coupled QD is 23. These values suggest that the coupling efficiency into ONF guided mode for the coupled QD is reduced by a factor of approximately 3, i.e., the ratio between PF and EF. From Figs. 1(c) and 1(d), this may correspond to an axially polarized dipole (*Z* pol). Note that for a radial dipole such a reduction factor is much higher than 10. From the Γ_{SP} and PL decay times τ_0 , we estimate a coupling efficiency ($\eta = \Gamma_{SP}\tau_0$) of 3.2% and 11% for the coupled and uncoupled QDs, assuming 100% quantum efficiency. The coupling efficiency of the coupled QD may be further improved by combining it with a moderate finesse ONF cavity [44–46].

From SEM images, we find that the single GNRs are always aligned along the ONF axis with a typical range of angle of $\pm 20^\circ$. This may be due to the surface forces [41]. We also perform simulations for different orientations of the GNR axis. Simulation results suggest that such a small angle does not significantly affect the performance of the device. It can be understood as the QD emission is strongly enhanced and polarized in the presence of GNR. The change in the orientation of the GNR axis will not affect the PF considering the dipole orientations with respect to the GNR axis. However, the projection of the dipole emission into ONF guided modes may change. This may induce a rotation of the polarization axis, but will not affect the DOP significantly [41]. For a typical angle of $\pm 25^\circ$, we numerically estimate a DOP of 98.2%.

Regarding the purity of the SPS, the $g^2(0)$ values for coupled QDs are higher than that for uncoupled QDs [see Fig. 5(a)]. This may be related to the residual multiphoton emission. On the other hand, we find that for much shorter PL decay times $g^2(0)$ values show an increasing trend. This may be due to the possible re-excitation of the QD, leading to emission of more than one photon per excitation pulse [47–49].

The blinking in the photon-count rate [Fig. 5(c)] of single QDs reveals that the emission switches between the exciton state and charged exciton (trion) state of the QD [42,50,51]. The strong blinking behavior in the photon-count rate of uncoupled QD is due to the reduced quantum efficiency for the trion [42,52,53]. In contrast, the photon-count rate of coupled QD [Fig. 5(d)] shows strongly suppressed blinking, indicating a high radiative recombination rate of QDs in the presence of GNR. The reason for suppressed blinking is that LSPR of GNR significantly increases the radiative decay rate of the coupled QD. The enhancement of the radiative decay rate sufficiently competes with the nonradiative processes and transition to trion state, leading to suppressed blinking. The present observations of the strongly suppressed blinking are in line with the previous report of CdSe/ZnS QDs in the proximity of gold nanorod and nanoantenna [22,54,55].

VI. CONCLUSION

In conclusion, we demonstrate a fiber in-line SPS based on plasmon-enhanced emission into ONF guided modes. We show that emission properties of single QDs can be strongly enhanced in the presence of GNRs leading to a bright and strongly polarized single-photon emission efficiently coupled to the guided modes of the ONF and eventually to a SMF. In this hybrid system by combining GNR and ONF, one can take the advantages of both state-of-the-art field confinement and low-loss propagation of single photons in fiber guided modes. The localized surface plasmon field of GNR significantly improves the emission properties of single QDs (brightness, DOP, suppressed blinking) and the quality of SPS. Coupling the single photons into ONF-guided modes enables automatic and alignment-free coupling to a SMF leading to a fiber-coupled SPS. The polarized and fiber-coupled single photons can be implemented for potential applications in quantum photonics.

ACKNOWLEDGMENTS

We acknowledge Kohzo Hakuta and Makoto Morinaga for fruitful discussions. We thank Mark Sadgroove for the SEM measurements. We acknowledge the contributions of Akiharu Miyanaga, Kazunori Iida and Emi Tsutsumi, in the preparation of the thick shell quantum dot samples. K.M.S. and K.P.N. acknowledge support from Deltafiber.jp Ltd. K.P.N. acknowledges support from a grant-in-aid for scientific research (Grant No. 21H01011) from the Japan Society for the Promotion of Science (JSPS). R.Y. acknowledges support from the Institute of Eminence (IoE) grant at the University of Hyderabad, India (File No. RC2-21-019).

Note added.—We have become aware of a related demonstration of plasmon-enhanced coupling of single photons into optical fiber [56].

[1] H. J. Kimble, The quantum internet, *Nature* **453**, 1023 (2008).
 [2] J. O'Brien, A. Furusawa, and J. Vuckovic, Photonic quantum technologies, *Nat. Photon* **3**, 687 (2009).
 [3] M. A. Nielsen and I. L. Chuang, *Quantum Computation and Quantum Communication* (Cambridge University Press, Cambridge, 2000).
 [4] N. Gisin, G. Ribordy, W. Tittel, and H. Zbinden, Quantum cryptography, *Rev. Mod. Phys.* **74**, 145 (2002).
 [5] I. Aharonovich, D. Englund, and M. Toth, Solid-state single-photon emitters, *Nat. Photonics* **10**, 631 (2016).
 [6] P. Senellart, G. Solomon, and A. White, High-performance semiconductor quantum-dot single-photon sources, *Nat. Nanotechnol.* **12**, 1026 (2017).

[7] C. H. Bennett and G. Brassard, Quantum cryptography: Public key distribution and coin tossing, International Conference on Computers, Systems and Signal Processing, Bangalore, India, Dec 9-12, (1984).
 [8] K. Takemoto, Y. Nambu, T. Miyazawa, Y. Sakuma, T. Yamamoto, S. Yoroza, and Y. Arakawa, Quantum key distribution over 120 km using ultrahigh purity single-photon source and superconducting single-photon detectors, *Sci. Rep.* **5**, 14383 (2015).
 [9] P. Michler, A. Kiraz, C. Becher, W. Schoenfeld, P. Petroff, L. Zhang, E. Hu, and A. Imamoglu, A quantum dot single-photon turnstile device, *Science* **290**, 2282 (2000).
 [10] Y.-S. Park, J. Lim, and V. I. Klimov, Asymmetrically strained quantum dots with non-fluctuating single-dot emission spectra and subthermal room-temperature linewidths, *Nat. Mater.* **18**, 249 (2019).
 [11] X. Lin, X. Dai, C. Pu, Y. Deng, Y. Niu, L. Tong, W. Fang, Y. Jin, and X. Peng, Electrically-driven single-photon sources based on colloidal quantum dots with near-optimal anti-bunching at room temperature, *Nat. Commun.* **8**, 1132 (2017).
 [12] S. E. Thomas, M. Billard, N. Coste, S. C. Wein, Priya, H. Ollivier, O. Krebs, L. Tazaïrt, A. Harouri, A. Lemaitre, I. Sagnes, C. Anton, L. Lanco, N. Somaschi, J. C. Lored, and P. Senellart, Bright Polarized Single-Photon Source Based on a Linear Dipole, *Phys. Rev. Lett.* **126**, 233601 (2021).
 [13] R. S. Daveau, K. C. Balram, T. Pregolato, J. Liu, E. H. Lee, J. D. Song, V. Verma, R. Mirin, S. W. Nam, L. Midolo, S. Stobbe, K. Srinivasan, and P. Lodahl, Efficient fiber-coupled single-photon source based on quantum dots in a photonic-crystal waveguide, *Optica* **4**, 178 (2017).
 [14] C.-M. Lee, M. A. Buyukkaya, S. Aghaeimeibodi, A. Karasahin, C. J. K. Richardson, and E. Waks, A fiber-integrated nanobeam single photon source emitting at telecom wavelengths, *Appl. Phys. Lett.* **114**, 171101 (2019).
 [15] M. J. Burek, C. Meuwly, R. E. Evans, M. K. Bhaskar, A. Sipahigil, S. n Meesala, B. Machielse, D. D. Sukachev, C. T. Nguyen, J. L. Pacheco, E. Bielejec, M. D. Lukin, and M. Lončar, Fiber-Coupled Diamond Quantum Nanophotonic Interface, *Phys. Rev. Appl.* **8**, 024026 (2017).
 [16] A. Sipahigil, R. E. Evans, D. D. Sukachev, M. J. Burek, J. Borregaard, M. K. Bhaskar, C. T. Nguyen, J. L. Pacheco, H. A. Atikian, C. Meuwly, R. M. Camacho, F. Jelezko, E. Bielejec, H. Park, M. Loncar, and M. D. Lukin, An integrated diamond nanophotonics platform for quantum-optical networks, *Science* **354**, 847 (2016).
 [17] C. Sönnichsen, T. Franzl, T. Wilk, G. von Plessen, J. Feldmann, O. Wilson, and P. Mulvaney, Drastic Reduction of Plasmon Damping in Gold Nanorods, *Phys. Rev. Lett.* **88**, 077402 (2002).
 [18] R. Esteban, T. V. Teperik, and J. J. Greffet, Optical Patch Antennas for Single Photon Emission using Surface Plasmon Resonances, *Phys. Rev. Lett.* **104**, 026802 (2010).
 [19] G. M. Akselrod, C. Argyropoulos, T. B. Hoang, C. Ciraci, C. Fang, J. Huang, D. R. Smith, and M. H. Mikkelsen, Probing the mechanisms of large Purcell enhancement in plasmonic nanoantennas, *Nat. Photonics* **8**, 835 (2014).
 [20] P. Wang, Y. Wang, Z. Yang, X. Guo, X. Lin, X.-C. Yu, Y.-F. Xiao, W. Fang, L. Zhang, G. Lu, Q. Gong, and L. Tong, Single-band 2-nm-line-width plasmon resonance in a strongly coupled Au nanorod, *Nano Lett.* **15**, 7581 (2015).

- [21] T. B. Hoang, G. M. Akselrod, and M. H. Mikkelsen, Ultrafast room-temperature single photon emission from quantum dots coupled to plasmonic nanocavities, *Nano Lett.* **16**, 270 (2016).
- [22] Y. He, J. Chen, R. Liu, Y. Weng, C. Zhang, Y. Kuang, X. Wang, L. Guo, and X. Ran, Suppressed Blinking and Polarization-dependent emission enhancement of single ZnCdSe/ZnS dot coupled with Au nanorods, *ACS Appl. Mater. Interfaces* **14**, 12901 (2022).
- [23] L. Tong, R. R. Gattass, J. B. Ashcom, S. He, J. Lou, M. Shen, I. Maxwell, and E. Mazur, Subwavelength-diameter silica wires for low-loss optical wave guiding, *Nature* **426**, 816 (2003).
- [24] F. L. Kien, S. D. Gupta, V. I. Balykin, and K. Hakuta, Spontaneous emission of a cesium atom near a nanofiber: Efficient coupling of light to guided modes, *Phys. Rev. A* **72**, 032509 (2005).
- [25] T. Nieddu, V. Gokhroo, and S. Nic Chormaic, Optical nanofibres and neutral atoms, *J. Opt.* **18**, 053001 (2016).
- [26] P. Solano, J. A. Grover, J. E. Homan, S. Ravets, F. K. Fatemi, L. A. Orozco, and S. L. Rolston, Optical nanofibers: A new platform for quantum optics, *Adv. At. Mol. Opt. Phys.* **66**, 439 (2017).
- [27] K. P. Nayak, M. Sadgrove, R. Yalla, F. L. Kien, and K. Hakuta, Nanofiber quantum photonics, *J. Opt.* **20**, 073001 (2018).
- [28] K. P. Nayak, P. N. Melentiev, M. Morinaga, F. L. Kien, V. I. Balykin, and K. Hakuta, Optical nanofiber as an efficient tool for manipulating and probing atomic fluorescence, *Opt. Express* **15**, 5431 (2007).
- [29] S. Kato and T. Aoki, Strong Coupling Between a Trapped Single Atom and an All-Fiber Cavity, *Phys. Rev. Lett.* **115**, 093603 (2015).
- [30] K. P. Nayak, J. Wang, and J. Keloth, Real-Time Observation of Single Atoms Trapped and Interfaced to a Nanofiber Cavity, *Phys. Rev. Lett.* **123**, 213602 (2019).
- [31] Y. Meng, C. Liedl, S. Pucher, A. Rauschenbeutel, and P. Schneeweiss, Imaging and Localizing Individual Atoms Interfaced with a Nanophotonic Waveguide, *Phys. Rev. Lett.* **125**, 053603 (2020).
- [32] L. Liebermeister, F. Petersen, A. V. Münchow, D. Burchardt, J. Hermelbracht, T. Tashima, A. W. Schell, O. Benson, T. Meinhardt, A. Krueger, A. Stiebeiner, A. Rauschenbeutel, H. Weinfurter, and M. Weber, Tapered fiber coupling of single photons emitted by a deterministically positioned single nitrogen vacancy center, *Appl. Phys. Lett.* **104**, 031101 (2014).
- [33] R. Yalla, Y. Kojima, Y. Fukumoto, H. Suzuki, O. Ariyada, K. M. Shafi, K. P. Nayak, and K. Hakuta, Integration of silicon-vacancy centers in nanodiamonds with an optical nanofiber, *Appl. Phys. Lett.* **120**, 241102 (2022).
- [34] M. Fujiwara, K. Toubaru, T. Noda, H.-Q. Zhao, and S. Takeuchi, Highly efficient coupling of photons from nanoemitters into single-mode optical fibers, *Nano Lett.* **11**, 4362 (2011).
- [35] R. Yalla, F. L. Kien, M. Morinaga, and K. Hakuta, Efficient Channeling of Fluorescence Photons from Single Quantum Dots into Guided Modes of Optical Nanofiber, *Phys. Rev. Lett.* **109**, 063602 (2012).
- [36] S. Pierini, M. D'Amato, M. Goyal, Q. Glorieux, E. Giacobino, E. Lhuillier, C. Coureau, and A. Bramati, Highly photostable perovskite nanocubes: Toward integrated single photon sources based on tapered nanofibers, *ACS Photonics* **7**, 2265 (2020).
- [37] A. W. Schell, H. Takashima, T. T. Tran, I. Aharonovich, and S. Takeuchi, Coupling quantum emitters in 2D materials with tapered fibers, *ACS Photonics* **4**, 761 (2017).
- [38] S. M. Skoff, D. Papencordt, H. Schaufert, B. C. Bayer, and A. Rauschenbeutel, Optical-nanofiber-based interface for single molecules, *Phys. Rev. A* **97**, 043839 (2018).
- [39] K. M. Shafi, K. P. Nayak, A. Miyanaga, and K. Hakuta, Efficient fiber in-line single photon source based on colloidal single quantum dots on an optical nanofiber, *Appl. Phys. B* **126**, 58 (2020).
- [40] F. L. Kien, J. Q. Liang, K. Hakuta, and V. I. Balykin, Field intensity distributions and polarization orientations in a vacuum-clad subwavelength-diameter optical fiber, *Opt. Commun.* **242**, 445 (2004).
- [41] M. Joos, C. Ding, V. Loo, G. Blanquer, E. G. A. Bramati, V. Krachmalnicoff, and Q. Glorieux, Polarization Control of Linear Dipole Radiation using an Optical Nanofiber, *Phys. Rev. Appl.* **9**, 064035 (2018).
- [42] K. M. Shafi, W. Luo, R. Yalla, K. Iida, E. Tsutsumi, A. Miyanaga, and K. Hakuta, Hybrid system of an optical nanofiber and a single quantum dot operated at cryogenic temperatures, *Sci. Rep.* **8**, 13494 (2018).
- [43] R. Yalla, K. P. Nayak, and K. Hakuta, Fluorescence photon measurements from single quantum dots on an optical nanofiber, *Opt. Express* **20**, 2932 (2012).
- [44] R. Yalla, M. Sadgrove, K. P. Nayak, and K. Hakuta, Cavity Quantum Electrodynamics on a Nanofiber using a Composite Photonic Crystal Cavity, *Phys. Rev. Lett.* **113**, 143601 (2014).
- [45] A. W. Schell, H. Takashima, S. Kamioka, Y. Oe, M. Fujiwara, O. Benson, and S. Takeuchi, Highly efficient coupling of nanolight emitters to a ultra-wide tunable nanofiber cavity, *Sci. Rep.* **5**, 9619 (2016).
- [46] F. L. Kien and K. Hakuta, Cavity-enhanced channeling of emission from an atom into a nanofiber, *Phys. Rev. A* **80**, 053826 (2009).
- [47] E. Peter, S. Laurent, J. Bloch, J. Hours, S. Varoutsis, I. Robert-Philip, A. Beveratos, A. Lemaître, A. Cavanna, G. Patriarche, and P. Senellart, Fast radiative quantum dots: From single to multiple photon emission, *Appl. Phys. Lett.* **90**, 223118 (2007).
- [48] S. Ates, I. Agha, A. Gulinatti, I. Rech, A. Badolato, and K. Srinivasan, Improving the performance of bright quantum dot single photon sources using temporal filtering via amplitude modulation, *Sci. Rep.* **3**, 1397 (2013).
- [49] K. Y. Kim, C. J. K. Richardson, E. Waks, and J. H. Kim, Temporal shaping of single photons by engineering exciton dynamics in a single quantum dot, *APL Photonics* **6**, 080801 (2021).
- [50] Y. Louyer, L. Biadala, P. Tamarat, and B. Lounis, Spectroscopy of neutral and charged exciton states in single CdSe/ZnS nanocrystals, *Appl. Phys. Lett.* **96**, 203111 (2010).
- [51] C. Javaux, B. Mahler, B. Dubertret, A. Shabaev, A. V. Rodina, A. L. Efros, D. R. Yakovlev, F. Liu, M. Bayer, G.

- Camps, L. Biadala, S. Buil, X. Quelin, and J-P. Hermier, Thermal activation of non-radiative Auger recombination in charged colloidal nanocrystals, *Nat. Nanotech.* **8**, 206 (2013).
- [52] Y. S. Park, W. K. Bae, J. M. Pietryga, and V. I. Klimov, Auger recombination of biexcitons and negative and positive trions in individual quantum dots, *ACS Nano* **8**, 7288 (2014).
- [53] D. E. Gómez, J. Embden, P. Mulvaney, M. J. Fernée, and H. R. Dunlop, Exciton-trion transitions in single CdSe-CdS core-shell nanocrystals, *ACS Nano* **3**, 2281 (2009).
- [54] X. Ma, H. Tan, T. Kipp, and A. Mews, Fluorescence enhancement, blinking suppression, and gray states of individual semiconductor nanocrystals close to gold nanoparticles, *Nano Lett.* **10**, 4166 (2010).
- [55] Q. Jiang, P. Roy, J. B. Claude, and J. Wenger, Single photon source from a nanoantenna-trapped single quantum dot, *Nano Lett.* **21**, 7030 (2021).
- [56] M. Sugawara, Y. Xuan, Y. Mitsumori, K. Edamatsu, and M. Sadgrove, Plasmon-enhanced single photon source directly coupled to an optical fiber, *Phys. Rev. Res.* **4**, 043146 (2022).